Microstructure characteristics of laser forming repaired Ti60 alloy

Yanhong Liu (刘彦红), Jing Chen (陈 静)*, Qiang Zhang (张 强), Lei Xue (薛 蕾), Xin Lin (林 鑫), and Weidong Huang (黄卫东)

State Key Laboratory of Solidification Processing, Northwestern Polytechnical University, Xi'an 710072, China

**Corresponding author: phd2003cjj@nwpu.edu.cn*

Received December 14, 2010; accepted March 4, 2011; posted online May 18, 2011

The microstructure characteristics of laser forming repaired (LFR) Ti60 (Ti-5.6Al-4.8Sn-2Zr-1Mo-0.35Si-0.3Nb) as-deposited and annealed samples are analyzed. The microstructure of as-deposited repaired zone (RZ) consists of epitaxial columnar prior β grains, in which fine woven α laths and β-phase between α laths exist. The heat-affected zone (HAZ) experiences a continuous microstructural transition from duplex microstructure of the base metal zone (BMZ) to the microstructure of RZ. The presence of silicide precipitates is observed in both RZ and BMZ in an annealed sample by transmission electron microscopy. They are identified as (Ti, Zr)$_6$Si$_3$ distributed mainly at the α/β interface with the size of 100−300 nm. The fine α_2 precipitates are detected in BMZ by electron diffraction; there was no α_2 detected in RZ.

OCIS codes: 140.3390, 160.3900, 350.3390.

doi: 10.3788/COL201109.071402.

Ti60 (Ti-5.6Al-4.8Sn-2Zr-1Mo-0.35Si-0.3Nb) is a near-α titanium alloy with good elevated temperature properties[1−4]. It has been identified as a candidate material for the fifth and sixth blisks of aeroengine compressors. Blisk repair has become one of the key technologies in the application of the new generation aeroengine due to the frequent occurrence of machine damage and problems with the aeroengine's service. Based on add-material manufacture principles, laser forming repaired (LFR)[5−8] can be used to repair damaged parts rapidly and is capable of size and properties recovery. Therefore, LFR is an advanced technology suitable for blisk repair. Analysis on the microstructure of LFR Ti60 serves as the basis of the application of LFR Ti60 blisk.

Preliminary studies on LFR Ti60 have been carried out in recent years[9,10]. Dense metallurgical bonding between repaired zone (RZ) and base metal zone (BMZ) was found[9], and the HAZ microstructure changed from the duplex microstructure of BMZ to the basketweave microstructure of RZ. Wang *et al*. found that the microstructure of LFR Ti60 was composed of directionally solidified columnar grains and the inner sides of the columnar grains were made of a fine cellular structure[10].

Silicon was added into titanium alloy such as Ti60 and IMI834 to improve high temperature properties. Thus, silicides were observed frequently in these alloys[11−14]. Recent research found that silicides played a positive role in strengthening the soft β layer in IMI834[15]. However, according to Ref. [16], the coarse, incoherent silicides in IMI834 were responsible for the decrease in yield and tensile strength. The effective role of coarse silicide precipitates on strengthening cannot compensate for the decrease in solid solution strengthening due to the depletion of the potential solid solution strengtheners Si and Zr from the matrix. Another precipitate in Ti60 alloy is the intermetallic α_2, whose presence in the matrix of Ti alloy has been reported to result in a significant loss of ductility and fracture toughness[17,18]. Generally, this has been attributed to an increased tendency of intense planar slip in the α matrix during deformation.

However, research on the microstructure of LFR Ti60 remains minimal, especially on the main precipitate silicides and α_2 in LFR Ti60. Hence, we investigate the microstructure characteristics of LFR Ti60 in both as-deposited and annealed states.

The LFR system consisted of a 5-kW continuous-wave (CW) CO_2 laser, a four-axis numerical control working table, and a powder feeder with a coaxial nozzle. The experiments were conducted inside a controlled atmosphere cabinet filled with argon gas. Ti60 powders fabricated by the plasma rotation electrode process (PREP) were used as cladding materials. To eliminate the moisture trapped in the powders, the powders were dried in a vacuum oven for 4 h. A 16×10×5 (mm) substrate was cut from a Ti60 wrought billet. The substrate surfaces were polished with sandpaper and cleaned thoroughly with acetone. The processing parameters used in the experiments are shown in Table 1. The dimension of the LFR sample was 15×10×15 (mm). Subsequently, the sample was evenly divided into two parts lengthwise. Each part was composed of RZ, HAZ, and BMZ. Annealing heat treatment was necessary because residual stresses existed in the LFR samples. The annealing heat treatment specifications were 500 °C and 4 h/FC (furnace cooling). Microstructural examinations were performed using an OLYMPUS-PMG3 optical microscope, a TESCAN VEGA II

Table 1. Parameters of the LFR Process

Laser Power (kW)	1.6–1.8
Scanning Velocity (mm/s)	4
Spot Diameter (mm)	1.5–2.3
Powder Feed Rate (g/min)	1–2
Overlapping Rate (%)	45
Shielding Gas Flow (L/min)	2–4
Increment of Z Axis (mm)	0.2

 © 2011 Chinese Optics Letters

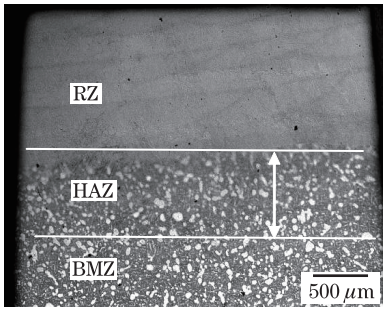

Fig. 1. Optical micrograph of laser forming as-deposited repaired sample.

scanning electron microscope, and a TECNAI F 30G^2 transmission electron microscope (TEM). The investigations of scanning transmission electron microscopy (STEM) and high resolution electron microscopy (HREM) were conducted with a TECNAI F 30G^2 TEM operating at 300 kV.

An optical micrograph of the as-deposited LFR sample is shown in Fig. 1. The macrostructure of the LFR sample consists of RZ, BMZ, and HAZ. Dense metallurgical bonding formed between RZ and BMZ can be observed.

The macrostructure of the main body of RZ is shown in Fig. 2. A continuously epitaxial columnar prior-β cellu-lar growth across several deposit layers can be observed. The growth direction is along the deposition and slightly inclines toward the laser scanning direction. The average cellular spacing is approximately 300 μm. During the process of laser cladding, the highest temperature gradient is produced at the bottom of the molten pool and its direction is perpendicular to the laser scanning direction, i.e., normal to the base metal. However, the direction of the temperature gradient changes from perpendicular at the bottom of the molten pool to that along the laser scanning direction at the top of the molten pool. Therefore, the growth of prior-β columnar crystals is slightly tilted toward the laser scanning direction. Layer bands structure can be seen from Fig. 2(a) as well. The coarsening of α laths due to reheating during the deposition of subsequent layers accounts for the formation of layer bands.

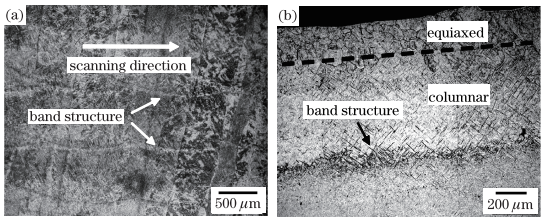

Fig. 2. OM macrostructure of laser forming as-deposited RZ. (a) Main body of RZ and (b) top of RZ.

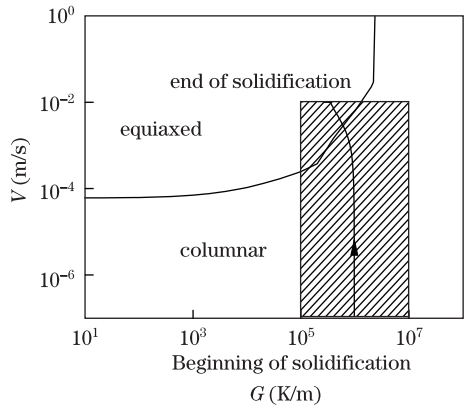

Fig. 3. CET curve of Ti60 alloy. Shadowed region showing the solidification parameters of LFR, G is temperature gradient and V is growth velocity.

Equiaxed grains were observed at the top of the last cladding layer, as shown in Fig. 2(b). This is evidence of the occurrence of columnar-to-equiaxed (CET) growth transition. The phenomenon can be explained by a CET curve, which is calculated by using the CET model[19]. The conditions under which CET will occur for alloy Ti60 were obtained. These are presented in Fig. 3. The shaded rectangle in Fig. 3 represents the range of solidification conditions existing in the LFR process, and the arrow path shows the progress of the solidification condition of the molten pool under the processing parameters used in the present study. Under the present conditions, columnar crystal growth will clearly dominate the initial process in the solidification of each cladding layer, and the CET condition will be reached at the end of solidification. This results in the formation of equiaxed grains at the top of the molten pool. However, due to the remelting effect of the successive laser passes, the equiaxed crystal zone is remelted and disappears. Thus, columnar growth becomes dominant throughout the deposit, while the equiaxed grains can only be seen at the top of the last cladding layer.

Figure 4 shows the microstructure in the columnar grains of RZ. The microstructure at the bottom of RZ is shown in Fig. 4(a). Fine woven α laths and the β-phase between α laths can be seen. The lath width and length are approximately 2−4 and 5−15 μm, respectively. Compared with the microstructure at the bottom of RZ, the micro structures at the top of RZ are markedly coarsened. Some α clusters grow along the prior-β grain boundary, as shown in Fig. 4(b). At the bottom of RZ, α phase is apt for nucleation due to a

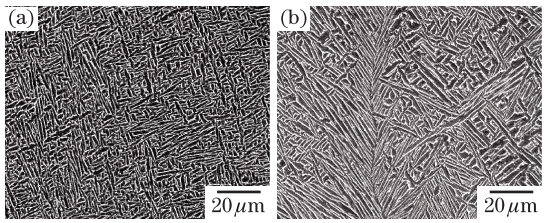

Fig. 4. SEM micrograph of laser forming as-deposited RZ. (a) Bottom of RZ and (b) top of RZ.

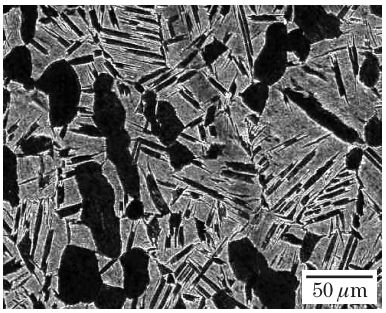

Fig. 5. SEM micrograph of BMZ in LFR as-deposited sample.

larger undercooling and a rapid cooling rate. As a result, nucleation rate increases and the textures of woven α laths are fine. However, with the continuation of laser cladding, undercooling and cooling rate decrease. Accordingly, nucleation rate decreases and α phase is prone to grow. Therefore, the microstructure is close to the Widmanstatten structure at the top of RZ.

The BMZ in the LFR as-deposited sample has a duplex microstructure, as shown in Fig. 5. Primary α grains are distributed in transformation β microstructure with the volume fraction of 25%−30%. The average size of primary α grains is 40 μm while α lamellar in transformation β microstructure has an average width of 4 μm and a length of 40 μm.

The width of HAZ in LFR sample is approximately 0.8 mm. Figure 6(a) shows the microstructure at the top of HAZ. The grain boundaries of primary α look fuzzy due to a considerable amount of fine α phases precipitated along the boundaries. Coarse α lamella in transformation β microstructure disappears and is replaced by fine α laths. The closer HAZ is to BMZ, the more similar their microstructures become. The microstructure at the bottom of HAZ shows no basic difference from that of BMZ, as shown in Fig. 6(b). A continuous microstructure transformation of HAZ from BMZ to RZ can be seen clearly, which results in good metallurgical bonding between BMZ and RZ.

As the cladding layers and base metal have undergone a very uneven effect from rapid heating and cooling during LFR, residual stresses in LFR sample are produced. In order to remove or adjust the residual stresses, anneal heat treatment is required for LFR sample. Annealing temperature should be low because the microstructure of BMZ could not be changed after annealing. In the present study, the annealing heat treatment parameters are 500 °C, 4 h/FC.

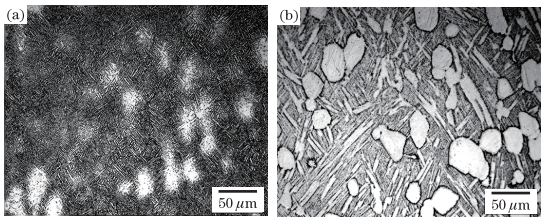

Fig. 6. Optical micrographs of HAZ in laser forming as-deposited repaired sample. (a) Top of HAZ and (b) bottom of HAZ.

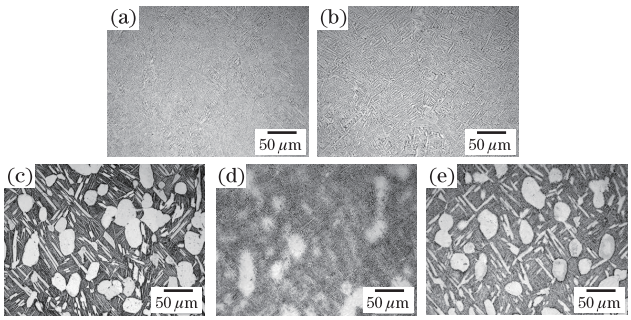

Fig. 7. Optical micrograph showing annealed microstructure of LFR sample. (a) Bottom of RZ, (b) top of RZ, (c) MBZ, (d) top of HAZ, and (e) bottom of HAZ.

The microstructure of the LFR sample shows no significant change after annealing, as shown in Fig. 7. However, long-term exposure to high temperature may result in the precipitation of silicide and α_2, and consequently, may lead to loss of ductility and fracture. This is similar to the results using other Ti alloys[13], which makes it necessary to investigate the precipitations. Silicide and α_2 are analyzed in RZ and BMZ by TEM, STEM, and HREM.

Figure 8(a) is a STEM micrograph of RZ. The white particles are silicides. Chemical composition of these silicides determined from EDX comprises 30.3 at.-% Si, 25.8 at.-% Zr, and 43.9 at.-% Ti. Selected area diffraction patterns (SADPs) obtained near a silicide particle are shown in Fig. 8(c). The weak diffraction pattern obtained from the silicide and illustrated in the inset of Fig. 8(c) shows that silicides have a hexagonal lattice. The microstructure shown in Fig. 8(d) is the dark field image of silicides. There are two hexagonal microstructural silicides in near-α Ti alloy, namely, (Ti, Zr)$_5$Si$_3$ and (Ti, Zr)$_6$Si$_3$. The lattice parameters of (Ti, Zr)$_5$Si$_3$ are a=0.780 nm and c=0.545 nm, while those of (Ti, Zr)$_6$Si$_3$ are a=0.701 nm and c=0.368 nm[1]. The silicides in the current study were identified as (Ti, Zr)$_6$Si$_3$ because they are consistent with the present electron diffraction.

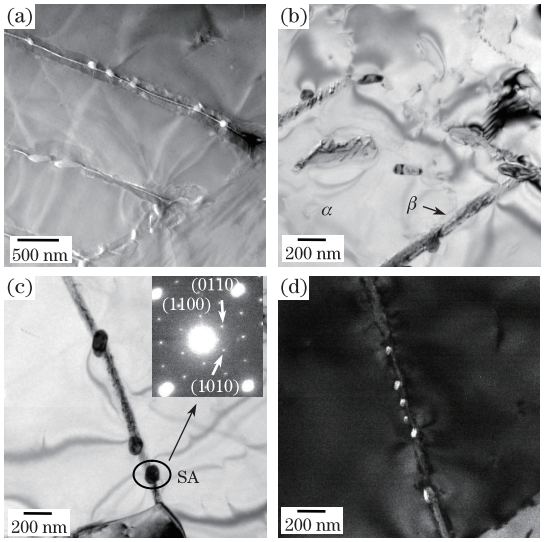

Fig. 8. Micrograph of silicides in RZ annealed. (a) STEM micrograph, (b) TEM micrograph of silicides, (c) bright field TEM of silicides with beam direction parallel to [0001] $_{\text{silicide}}$, and (d) dark field TEM micrograph with beam direction parallel to [0001] $_{\text{silicide}}$.

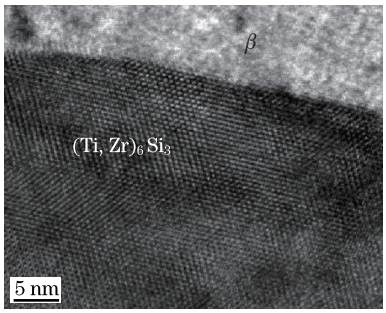

Fig. 9. HREM image showing two phases in annealed RZ: β and silicide.

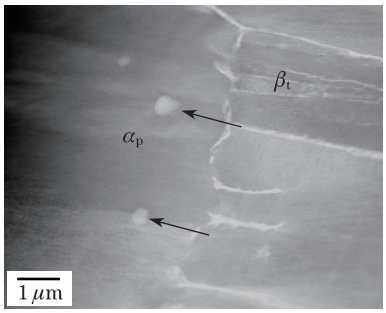

Fig. 10. STEM micrograph of silicides in annealed BMZ.

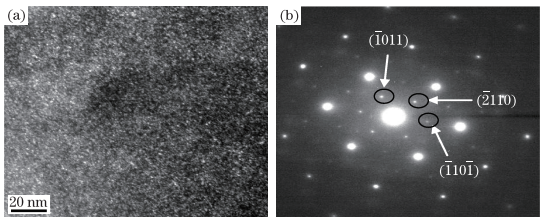

Fig. 11. α_2 in BMZ annealed. (a) Dark field TEM micrographs of α_2 and (b) super lattice of α_2.

In Fig. 9(b), silicides are distributed mainly at α/β interface, except for a few which are distributed in the α laths. The silicides are elliptical and have sizes within 100−300 nm. The boundaries of β and silicide can be seen from the HREM image (Fig. 9). Most probably, the large mismatch between β and silicide strengthened the soft β laths.

The white particles in Fig. 10 are silicides in BMZ. They are similar to those of RZ in terms of morphology and size. They are also distributed mainly at the α/β interface. However, the number of silicides in BMZ is significantly less than that of silicides in RZ.

There are no α_2 precipitates in RZ, and no superlattice spots detected by extensive TEM. On the other hand, α_2 precipitates can be observed in BMZ as shown in Fig. 11(a). The microstructure shown in Fig. 11(a) is the dark field image obtained from BMZ using a superlattice reflection from the α_2 phase. This is indicated by the circle in the SADP of Fig. 11(b). These α_2 precipitates are homogenously distributed in the α matrix and have an average size of 1−2 nm.

The precipitation of silicides and α_2 is related to heat treatment, process history, etc.[16] The annealing heat treatment (500 °C, 4 h/FC) shows no significant effect on precipitation because the annealing temperature is not high enough and time is not long enough[13]. Since RZ and BMZ are respectively acquired by LFR and forge, they are different in terms of process history before annealing. This could probably be the reason which led to the formation of different states in silicides and α_2.

In conclusion, the microstructure characteristics of LFR Ti60 alloy in both as-deposited and annealed states are investigated. LFR as-deposited sample consists of RZ, BMZ, and HAZ. A continuously epitaxial columnar prior-β cellular growth across several deposit layers in RZ, whose growth direction is along the deposition direction and slightly inclines toward the scanning direction, is achieved. Layer band structure and CET growth transition are observed as well. Moreover, fine woven α laths and the β-phase between laths are found to exist in columnar β grains. The microstructure of BMZ in LFR as-deposited sample is a duplex. HAZ successfully achieves microstructure transformation from BMZ to RZ, which results in metallurgical bonding between BMZ and RZ. The microstructure of LFR sample shows no significant change after annealing. The silicides, identified as $(Ti, Zr)_6Si_3$, are discovered in RZ, distributed mainly at α/β interface, with sizes within 100–300 nm. However, the number of silicides in BMZ is considerably less than the number in RZ. The α_2 precipitates, detected in BMZ and not in RZ, are homogenously distributed in the α matrix and have an average size of 1−2 nm.

This work was supported by the Research Fund of the State Key Laboratory of Solidification Processing (NWPU), China (No. 33-TP-2009), the National Natural Science Foundation of China (No. 50871089), and the Programme of Introducing Talents of Discipline to Universities of China (No. 08040).

References

1. S. Zhang, Q. Wang, Y. Liu, and R. Yang, Acta Metall. Sin. (in Chinese) **41,** 970 (2005).
2. Z. Chen, Q. Wang, J. Liu, Y. Li, K. Tang, J. Li, and T. Liu, Acta Metall. Sin. (in Chinese) **44,** 263 (2008).
3. G. Li, D. Li, Y. Liu, Q. Wang, S. Gao, and Q. Li, J. Aer. Mat. (in Chinese) **17,** 22 (1997).
4. W. Jia, W. Zeng, H. Yu, and Y. Zhou, Chin. J. Nonf Met. al. (in Chinese) **19,** 1033 (2009).
5. S. Zhang, X. Lin, J. Chen, and W. Huang, Chin. Opt. Lett. **7,** 498 (2009).
6. F. Zhang, J. Chen, H. Tan, X. Lin, and W. Huang, Chin. Opt. Lett. **7,** 222 (2009).
7. J. Wang, J. Chen, Y. Liu, X. Zhao, and F. Zhang, Chinese J. Lasers (in Chinese) **37,** 847 (2010).
8. J. Chen, S. Zhang, L. Xue, H. Yang, X. Lin, and W. Huang, Rare Metal Mat. Eng. (in Chinese) **36,** 475 (2007).
9. F. Zhang, J. Chen, L. Xue, X. Lin, and W. D. Huang, Appl. Lasers (in Chinese) **29,** 87 (2009).
10. B. Wang, S. Zhang, and H. Wang, Trans. Mat. Heat Treat. (in Chinese) **29,** 86 (2008).
11. S. D. Meshram and T. Mohandas, Mater. Design **31,** 2245 (2010).
12. N. Singh and V. Singh, Mat. Sci. Eng. A **485,** 1130 (2008).
13. X. D. Zhang, D. J. Evans, W. A. Baeslack, and H. L. Fraser, Mat. Sci. Eng. A **344,** 300 (2003).
14. M. Es-Souni, Mater. Charact. **46,** 365 (2001).
15. X. Wang, M. Jahazi, and S. Yue, Mat. Sci. and Eng. A **492,** 450 (2008).
16. K. V. Sai Srindh, N. Singh, and V. Singh, Mater. Sci. **30,** 595 (2007).
17. X. D. Zhang, J. M. K. Wiezorek, W. A. Baeslack III, D. J. Evans, and H. L. Fraser, Acta Mater. **46,** 4485 (1998).
18. T. Neeraj and M. J. Mills, Mat. Sci. Eng. A **319,** 415 (2001).
19. X. Lin, T. M. Yue, H. O. Yang, and W. D. Huang, Mat. Sci. Eng. A **391,** 325 (2005).